POLITECNICO
MILANO 1863

DIPARTIMENTO DI MECCANICA

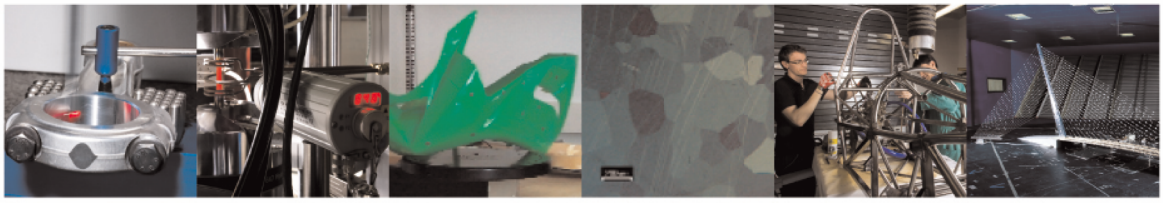

Indirect Model Predictive Control for a Grid-Tied Three-Level Neutral Point Clamped Converter with an LCL Filter

Mattia Rossi, Petros Karamanakos, and Francesco Castelli-Dezza, Member

This is a post-peer-review, pre-copyedit version of an article published in *IEEE Transactions on Industry Applications*. The final authenticated version is available online at: https://dx.doi.org/10.1109/TIA.2022.3152463

DIPARTIMENTO DI MECCANICA ■ POLITECNICO DI MILANO
via G. La Masa, 1 ■ 20156 Milano ■ EMAIL (PEC): pecmecc@cert.polimi.it
http://www.mecc.polimi.it
Rev. 0

Indirect Model Predictive Control for a Grid-Tied Three-Level Neutral Point Clamped Converter with an LCL Filter

Mattia Rossi, *Student Member, IEEE,* Petros Karamanakos, *Senior Member, IEEE,* and Francesco Castelli-Dezza, *Member, IEEE*.

***Abstract*—The paper presents a model predictive control (MPC) algorithm for a three-level neutral point clamped converter connected to the grid via an LCL filter. The proposed long-horizon MPC, formulated as a multi-criterion quadratic program (QP), simultaneously controls the grid and converter current as well as the filter capacitor voltage, while meeting the relevant grid standards. To achieve the latter, a carrier-based pulse width modulation (CB-PWM) stage is employed. Finally, soft constraints are included to ensure operation of the system within its safe operating limits, particularly with regards to a potential overcurrent or overvoltage trip during transient operation. The presented results verify the effectiveness of the proposed method.**

I. Introduction

Grid-tied converters are a key technology for the integration of renewable energy sources, scalable loads, and high-performance drives in the electrical grid. For medium-voltage (MV) applications, grid codes—such as the IEEE 519 [1] and the IEC 61000-2-4 [2] standards—impose tight limits on the amplitudes of the current and voltage harmonics injected at the point of common coupling (PCC). To this end, LCL filters are commonly used to interface the converters with the grid as they provide stronger harmonic attenuation along with a reduced size (i.e., lower cost) compared to, e.g., L filters. The LCL filter, however, introduces additional control challenges due to the higher order of the resulting system, i.e., besides the control of the grid current, the control of the converter current and capacitor voltage are needed. Moreover, the resonance introduced by the filter needs to be adequately damped to avoid current harmonics amplification, or, even, stability issues.

During the last decade, model predictive control (MPC) has gained popularity in the field of power electronics as a promising alternative to traditional control and modulation strategies [3]–[5]. Depending on whether a modulator is used, MPC is classified into two categories, i.e., direct MPC—also known as finite control set MPC (FCS-MPC)—and indirect MPC—also referred to as continuous control set MPC (CCS-MPC). FCS-MPC performs the control and modulation tasks in one computational stage, thus it directly generates the optimal switching signals. This implies that the controller operates the converter at a variable switching frequency, which results in non-deterministic harmonic spectra [6]. For grid-tied converters, this complicates the system design, e.g., it may lead to an overly conservative choice for the output filter, cooling system, and semiconductor devices, while meeting the grid standards becomes challenging.

Motivated by the above, this paper considers an indirect MPC for a three-level neutral point clamped (3L-NPC) converter connected to the grid via an LCL filter. By employing a carrier-based pulse width modulation (CB-PWM) stage the converter can be operated at a fixed switching frequency and generates deterministic harmonic spectra, with harmonic components limited to non-triplen odd integer multiplies of the fundamental frequency. Furthermore, by formulating the optimization problem underlying indirect MPC as a multi-criterion quadratic program (QP) several benefits follow. First, all primary control objectives, i.e., the control of the grid and converter current as well as of the filter capacitor voltage, are achieved and the relevant grid codes met, while the converter is operated at low switching frequency. Second, the computational complexity of the problem remains moderate, even when long horizons are utilized for improved system performance [7]. Regarding the latter, it is worth mentioning that they are particularly beneficial when higher-order systems—as the examined one—are of concern, see, e.g., [8], since it has been manifested that—when combined with full-state information—they can provide active damping without the need for additional damping loops. Third, by imposing hard constraints on the control input (i.e., the modulating signal) and soft constraints on the system output, operation within the safe operating area of the system—given as trip levels—is achieved. Hence, damage (or aging) of the hardware due to overvoltages and/or overcurrents can be avoided (reduced). Finally, owing to the QP formulation of the optimization problem, online solvers that are able to solve such problems on embedded hardware in a manner of microseconds, see, e.g., [9]–[11], can be employed, thus facilitating the real-time implementation of the controller.

II. Case Study

Consider the three-phase 3L-NPC converter connected to the grid via an intermediate LCL filter, as shown in Fig. 1(a). The filter is placed between the converter and the step-down transformer in order to reduce the harmonic distortions at the PCC. To keep the demonstration of the proposed method simple, the dc-link voltage is assumed to be constant $v_{\mathrm{dc}}(t) = V_{\mathrm{dc}}$ and balanced, thus, the neutral point potential N is fixed at zero. Since additional loads may be connected to the PCC, strict grid standards are imposed at this point. The IEEE 519 [1] and IEC 61000-2-4 [2] standards are

M. Rossi and F. Castelli-Dezza are with the Department of Mechanical Engineering, Politecnico di Milano, 20156 Milan, Italy, e-mail: [mattia.rossi, francesco.castellidezza]@polimi.it

P. Karamanakos is with the Faculty of Information Technology and Communication Sciences, Tampere University, 33101 Tampere, Finland, e-mail: p.karamanakos@ieee.org.

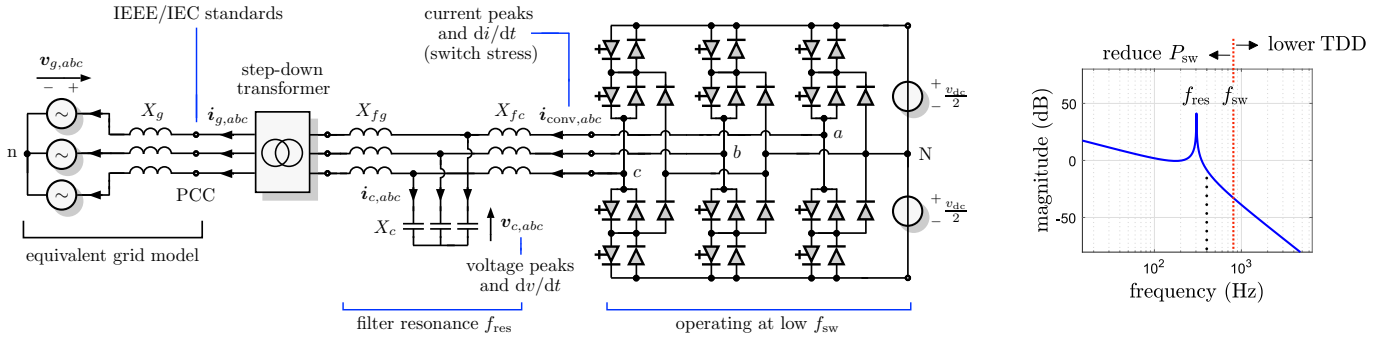

(a) (b)

Fig. 1. (a) Grid-tied 3L-NPC converter, based on IGCTs, with an LCL filter. The potential root cause of faults is also highlighted. (b) Frequency response of the LCL filter. The filter resonance f_{res} and switching frequency f_{sw} are shown. The latter should be as low as possible, while keeping the system stability.

considered in this paper. In addition, physical limitations, such as voltage peaks and $\mathrm{d}v/\mathrm{d}t$ across the filter capacitor as well as current peaks and $\mathrm{d}i/\mathrm{d}t$ of the converter current (i.e., through the semiconductors) are considered and converter trip levels defined [12]. Moreover, given the MV target, the converter is required to operate at a low switching frequency and as close to the resonance frequency of the LCL filter as possible, without exciting the current harmonics close to the latter. In doing so, not only the power switching losses can be kept low, but also the produced grid current harmonics can abide by the aforementioned grid standards and potential stability issues avoided, while increasing the system reliability.

III. Controller Model

In the sequel, a mathematical description of the converter dynamics is derived in the $\alpha\beta$-reference frame. All variables given in the abc-plane $\boldsymbol{\xi}_{abc} = [\xi_a \ \xi_b \ \xi_c]^T$ are mapped into two-dimensional vectors $\boldsymbol{\xi}_{\alpha\beta} = [\xi_\alpha \ \xi_\beta]^T$ via the reduced Clarke transformation matrix $\boldsymbol{K}$ (i.e., without the common-mode component)

$$\boldsymbol{K} = \frac{2}{3}\begin{bmatrix} 1 & -\frac{1}{2} & -\frac{1}{2} \\ 0 & \frac{\sqrt{3}}{2} & -\frac{\sqrt{3}}{2} \end{bmatrix} . \tag{1}$$

Based on Fig. 1(a), the equivalent circuit of the system in consideration is derived in the $\alpha\beta$-plane.[1] Before doing so, all SI variables are normalized based on the rated values of the step-down transformer.[2] The voltage $\boldsymbol{v}_g(t)$ to the left of the PCC models the grid source, while $\boldsymbol{i}_g(t)$ is the grid current. The distribution lines are approximated by the grid resistance R_g and inductance L_g, which are assumed equal for all windings. The grid reactance is $X_g = \omega_g L_g$, where ω_g is the grid angular frequency. Likewise, the step-down transformer can be represented by its split series resistance R_t and leakage reactance X_t. The LCL filter is described by the grid-side resistance R_{fg} and reactance X_{fg}, the capacitor reactance[3] X_c and its internal resistance R_c as well as the converter-side resistance R_{fc} and reactance X_{fc}. The converter current

[1]Hereafter, to simplify the notation, the subscript $\alpha\beta$ is dropped from all vectors unless otherwise stated.

[2]According to Table I, the per unit (p.u.) system is established using the base quantities $V_B = \sqrt{2/3}V_R$, $I_B = \sqrt{2}I_R$, $S_B = S_R = (3/2)\,V_B I_B$, and $\omega_B = \omega_g = 2\pi f_g$, where V_R and I_R denote the (rated) rms line-to-line voltage and rms line current referred to the secondary side of the transformer.

[3]Strictly speaking, X_c denotes the inverse of the reactance, since it holds $\frac{1}{X_c} = \frac{1}{\omega_B C}\frac{1}{Z_B}$, where C is the capacitor.

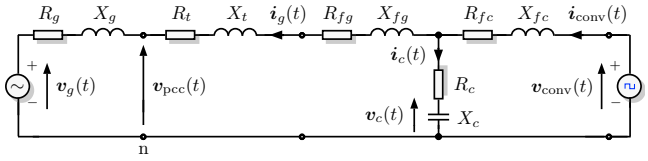

Fig. 2. Equivalent circuit (harmonic model) in the $\alpha\beta$-plane of the conversion scheme given inf Fig. 1(a). The PCC is denoted by the voltage $\boldsymbol{v}_{\text{pcc}}(t)$.

is $\boldsymbol{i}_{\text{conv}}(t)$ and $\boldsymbol{i}_c(t)$ is the current flowing through the filter capacitor branch, while $\boldsymbol{v}_c(t)$ is the capacitor voltage.[4]

A. LCL Filter Resonance and Grid Strength

The grid strength is characterized by the impedance ratio k_{XR} and the short-circuit ratio k_{sc}, which are defined as

$$k_{\text{XR}} = \frac{X_g}{R_g}\,, \quad k_{\text{sc}} = \frac{S_{\text{sc}}}{S_R} = \frac{V_R^2}{\sqrt{R_g^2 + X_g^2}}\frac{1}{S_R}\,. \tag{2}$$

The short-circuit power S_{sc} can be interpreted as the maximum power that the grid can provide to the PCC. According to Table I, ratios of $k_{\text{sc}} \approx 19.96$ and $k_{\text{XR}} \approx 10.02$ indicate a strong grid where the impedance seen at the PCC dominates over the grid impedance [5]. By lumping the resistances and reactances to the left of the LCL filter into the quantities $R = R_g + R_t + R_{fg}$ and $X = X_g + X_t + X_{fg}$ the filter resonances are defined as

$$f_{\text{res}} = f_B \frac{1}{\sqrt{X_c \frac{X_{fc}X}{X_{fc}+X}}}\,, \quad \widetilde{f}_{\text{res}} = f_B \frac{1}{\sqrt{X_c X}}\,, \tag{3}$$

where $f_B = \omega_B/(2\pi)$ is the base frequency. The dominant one is f_{res}, resulting by the interaction of the filter capacitor reactance X_c with the grid-side filter reactance X_{fc} and the equivalent total reactance X. The three resistors R, R_c and R_{fc} can be assumed negligible and, thus, they provide effectively no passive damping.

B. Physical Model of the System

According to the proposed indirect MPC approach, the controller output is the three-phase modulating signal $\boldsymbol{u}_{\text{ref},abc}(t) = [u_{\text{ref},a} \ u_{\text{ref},b} \ u_{\text{ref},c}]^T \in \boldsymbol{\mathcal{U}} = [-1,1]^3 \subset \mathbb{R}^3$. This relates to the ideal converter voltage $\boldsymbol{v}_{\text{conv,ref}}(t)$ via

$$\boldsymbol{v}_{\text{conv,ref}}(t) = \frac{V_{\text{dc}}}{2}\boldsymbol{K}\boldsymbol{u}_{\text{ref},abc}(t) = \frac{V_{\text{dc}}}{2}\boldsymbol{u}_{\text{ref}}(t)\,, \tag{4}$$

[4]Note that, currents flowing towards the grid are assumed to be positive.

while, the actual converter voltage $\boldsymbol{v}_{\mathrm{conv}}(t)$ approximates $\boldsymbol{v}_{\mathrm{conv,ref}}(t)$ through the 3L CB-PWM principle[5]. A phase disposition (PD) approach is considered in this paper because it results in lower harmonic distortions, see [13].

Given the equivalent circuit in Fig. 2, the system dynamics in the $\alpha\beta$-plane are given by the following continuous-time differential equations

$$X_{fc}\frac{\mathrm{d}\boldsymbol{i}_{\mathrm{conv}}(t)}{\mathrm{dt}} = -R_1\boldsymbol{i}_{\mathrm{conv}}(t) - \boldsymbol{v}_c(t) + R_c\boldsymbol{i}_g(t) + \boldsymbol{v}_{\mathrm{ref}}(t) \quad (5a)$$

$$X_c\frac{\mathrm{d}\boldsymbol{v}_c(t)}{\mathrm{dt}} = \boldsymbol{i}_c(t) = \boldsymbol{i}_{\mathrm{conv}}(t) - \boldsymbol{i}_g(t) \quad (5b)$$

$$X\frac{\mathrm{d}\boldsymbol{i}_g(t)}{\mathrm{dt}} = R_c\boldsymbol{i}_{\mathrm{conv}}(t) + \boldsymbol{v}_c(t) - R_2\boldsymbol{i}_g(t) - \boldsymbol{v}_g(t) \quad (5c)$$

$$\frac{\mathrm{d}\boldsymbol{v}_g(t)}{\mathrm{dt}} = \omega_g\begin{bmatrix}0 & -1\\ 1 & 0\end{bmatrix}\boldsymbol{v}_g(t)\,. \quad (5d)$$

Note that the above expression is derived on the assumption of a symmetrical balanced three-phase grid. Moreover, $R_1 = R_{fc} + R_c$ and $R_2 = R + R_c$ are introduced for notational simplification, while $\boldsymbol{v}_{\mathrm{conv,ref}}(t)$ is simply called $\boldsymbol{v}_{\mathrm{ref}}(t)$.

By defining $\boldsymbol{x}(t) = [\boldsymbol{i}_{\mathrm{conv}}^T(t)\ \boldsymbol{v}_c^T(t)\ \boldsymbol{i}_g^T(t)\ \boldsymbol{v}_g^T(t)]^T \in \mathbb{R}^8$, and $\boldsymbol{y}(t) = [\boldsymbol{i}_{\mathrm{conv}}^T(t)\ \boldsymbol{v}_c^T(t)\ \boldsymbol{i}_g^T(t)]^T \in \mathbb{R}^6$ as the state and output vectors, respectively, and $\boldsymbol{u}(t) = \boldsymbol{u}_{\mathrm{ref},abc}(t)$ as the control input, the continuous-time state-space representation is

$$\frac{\mathrm{d}\boldsymbol{x}(t)}{\mathrm{dt}} = \boldsymbol{F}\boldsymbol{x}(t) + \boldsymbol{G}\boldsymbol{u}(t) \quad (6a)$$

$$\boldsymbol{y}(t) = \boldsymbol{C}\boldsymbol{x}(t)\,, \quad (6b)$$

where $\boldsymbol{F} \in \mathbb{R}^{8\times8}$, $\boldsymbol{G} \in \mathbb{R}^{8\times3}$, and $\boldsymbol{C} \in \mathbb{R}^{6\times8}$ given by

$$\boldsymbol{F} = \begin{bmatrix} -\frac{R_1}{X_{fc}}\boldsymbol{I}_2 & -\frac{1}{X_{fc}}\boldsymbol{I}_2 & \frac{R_c}{X_{fc}}\boldsymbol{I}_2 & \boldsymbol{0}_{2\times2} \\ \frac{1}{X_c}\boldsymbol{I}_2 & \boldsymbol{0}_{2\times2} & -\frac{1}{X_c}\boldsymbol{I}_2 & \boldsymbol{0}_{2\times2} \\ \frac{R_c}{X}\boldsymbol{I}_2 & \frac{1}{X}\boldsymbol{I}_2 & -\frac{R_2}{X}\boldsymbol{I}_2 & -\frac{1}{X}\boldsymbol{I}_2 \\ \boldsymbol{0}_{2\times2} & \boldsymbol{0}_{2\times2} & \boldsymbol{0}_{2\times2} & \omega_g\begin{bmatrix}0 & -1\\ 1 & 0\end{bmatrix} \end{bmatrix}$$

$$\boldsymbol{G} = \frac{v_{\mathrm{dc}}}{2X_{fc}}\begin{bmatrix}\boldsymbol{I}_2 & \boldsymbol{0}_{2\times6}\end{bmatrix}^T\boldsymbol{K}, \quad \boldsymbol{C} = \begin{bmatrix}\boldsymbol{I}_6 & \boldsymbol{0}_{6\times2}\end{bmatrix}.$$

Note that since an ideal grid is assumed, the amplitude V_g and frequency ω_g of $\boldsymbol{v}_g(t)$ are constant, making $\boldsymbol{F}$ a time-invariant matrix.[6] Moreover, due to the assumption of a constant dc link, $\boldsymbol{G}$ is also time invariant. Finally, the dimension of the zero $\boldsymbol{0}$ and identity $\boldsymbol{I}$ matrices is given by their subscripts.

MPC requires the prediction model of the system to be in the discrete-time domain. The system dynamics, given by (6a) and (6b), are discretized using exact discretization with the sampling interval T_s. This yields

$$\boldsymbol{x}(k+1) = \boldsymbol{A}\boldsymbol{x}(k) + \boldsymbol{B}\boldsymbol{u}(k) \quad (8a)$$

$$\boldsymbol{y}(k) = \boldsymbol{C}\boldsymbol{x}(k)\,, \quad (8b)$$

with $\boldsymbol{A} = \mathbf{e}^{\boldsymbol{F}T_s}$ and $\boldsymbol{B} = -\boldsymbol{F}^{-1}(\boldsymbol{I}_4 - \boldsymbol{A})\boldsymbol{G}$, since $\boldsymbol{F}$ is nonsingular. Moreover, $\mathbf{e}$ is the matrix exponential, and $k \in \mathbb{N}$ denotes the discrete time step.

[5]The modulator computes the three-phase switch positions $\boldsymbol{u}_{\mathrm{abc}}$ to be applied at the converter, for which $3^3 = 27$ voltage vectors $\boldsymbol{u}_{\alpha\beta0}$ exist.

[6]Nevertheless, if the grid is subject to voltage imbalances, $\boldsymbol{v}_g(t)$ may be considered as an external disturbance to the system instead of a state. In doing so, $\boldsymbol{F}$ remains time invariant.

IV. Formulation of Long-Horizon MPC as a Quadratic Program

To address the control problem of the grid-tied 3L-NPC converter with an LCL filter, an indirect MPC approach is developed that aims to regulate the grid current $\boldsymbol{i}_g(t)$, converter current $\boldsymbol{i}_{\mathrm{conv}}(t)$ and capacitor voltage $\boldsymbol{v}_c(t)$ along their sinusoidal references. These reference values are computed based on the real $P_{\mathrm{in,ref}}(t)$ and reactive $Q_{\mathrm{in,ref}}(t)$ power requirements on the secondary side of the step-down transformer, with $Q_{\mathrm{in,ref}}(t) = 0$ at steady-state operation to achieve unity power factor (i.e., pf $= 1$). The ultimate goal is to produce a low total demand distortion (TDD) of $\boldsymbol{i}_g(t)$ and $\boldsymbol{v}_{\mathrm{pcc}}(t)$ as well as limit the amplitude of the associated harmonics to meet the relevant grid standards. Moreover, during power transients, very fast current and voltage responses have to be achieved, while keeping $\boldsymbol{i}_{\mathrm{conv}}(t)$ and $\boldsymbol{v}_c(t)$ within given bounds, designed as converter trip levels. To this end, soft constraints are implemented to introduce the physical limitations of the switching devices and passive components into the optimization problem.[7] Furthermore, hard constraints are imposed on the modulating signal/control input $\boldsymbol{u}_{\mathrm{ref},abc}(t) = \boldsymbol{u}(t)$ to ensure that its amplitude does not exceed the carrier signals bounds. Finally, given the MV system in consideration, all objectives should be met while operating the system at low device switching frequency, i.e., f_{sw} of a few hundred hertz, to keep the switching power losses low.

A. Objective Function Formulation

Given a prediction horizon of N_p time steps, the aforementioned control objectives are mapped into a scalar by the objective function[8]

$$J(k) = \sum_{\ell=k}^{k+N_p-1}\|\boldsymbol{y}_{\mathrm{ref}}(\ell+1) - \boldsymbol{y}(\ell+1)\|_{\boldsymbol{Q}}^2 + \lambda_u\|\Delta\boldsymbol{u}(\ell)\|_2^2\,. \quad (9)$$

According to (9), the first term is the output tracking error term $\boldsymbol{y}_{\mathrm{err}}(\ell+1) = \boldsymbol{y}_{\mathrm{ref}}(\ell+1) - \boldsymbol{y}(\ell+1)$, which denotes the deviation of the output variables $\boldsymbol{y}$ from their reference values $\boldsymbol{y}_{\mathrm{ref}}$, defined as $\boldsymbol{y}_{\mathrm{ref}} = [\boldsymbol{i}_{\mathrm{conv,ref}}^T\ \boldsymbol{v}_{c,\mathrm{ref}}^T\ \boldsymbol{i}_{g,\mathrm{ref}}^T]^T$. The latter are calculated based on a steady-state analysis of the system for a desired real and reactive power, $P_{\mathrm{in,ref}}$ and $Q_{\mathrm{in,ref}}$, respectively. Note that the output error term is weighted with the positive semidefinite matrix $\boldsymbol{Q} \succeq 0$.

Regarding the second term in (9), it denotes the control effort $\Delta\boldsymbol{u}(\ell) = \boldsymbol{u}(\ell) - \boldsymbol{u}(\ell-1)$, and it is introduced to enable smoother control by penalizing the control input changes between consecutive time instants. Moreover, $\lambda_u \in \mathbb{R}^{++}$ is the associated weighting factor. Given that, the optimization variable is the sequence of the three-phase modulating signals over the N_p-step prediction horizon, i.e.,

$$\boldsymbol{U}(k) = \left[\boldsymbol{u}^T(k)\ \boldsymbol{u}^T(k+1)\ \ldots\ \boldsymbol{u}^T(k+N_p-1)\right]^T, \quad (10)$$

the control effort term $\Delta\boldsymbol{u}(\ell)$ is a real-valued vector (rather than an integer as for FCS-MPC), i.e., $\Delta\boldsymbol{u} \in \mathbb{R}^3$.

[7]Reliability prediction in MV systems identifies filter capacitor banks and semiconductor switches as two of the most fragile elements [12].

[8]Note that $\|\boldsymbol{\xi}\|_{\boldsymbol{Q}}^2 = \boldsymbol{\xi}^T\boldsymbol{Q}\boldsymbol{\xi}$ denotes the squared norm of a vector $\boldsymbol{\xi}$ weighted with the matrix $\boldsymbol{Q}$.

B. Hard and Soft Constraints

Since a modulator is used to translate the modulating signal into switching commands, hard constraints should be imposed on $\boldsymbol{u}(\ell)$. Thus, given the amplitude of the carrier signals, the modulating signal is bounded between -1 and 1 for each prediction horizon time step $\ell = k, k+1, \ldots, k+N_p-1$, i.e.,

$$-\mathbf{1}_3 \preceq \boldsymbol{u}(\ell) \preceq \mathbf{1}_3\,. \tag{11}$$

Note that $\mathbf{1}$ is a vector with all entries equal to one and of dimensions as indicated by the subscript. Introducing the matrix $\boldsymbol{V} = [\,\boldsymbol{I}_3\ -\boldsymbol{I}_3\,]^T$, constraint (11) can be written as

$$\boldsymbol{V}\boldsymbol{u}(\ell) \preceq \mathbf{1}_6\,. \tag{12}$$

As hard constraints on state and/or output variables might cause feasibility issues, we introduce soft constraints on $\boldsymbol{y}(\ell)$ to restrict the operation of the 3L-NPC converter system within the safe operating area. Such constraints can be formulated as (in)equalities that can be relaxed using slack variables $\xi \in \mathbb{R}^+$. The latter represent the degree of the constraint violation, thus, ξ have to be minimized. For example, the soft constraints on the converter current of phase $x \in \{a, b, c\}$ at time step ℓ are of the form [14]

$$\xi_{\mathrm{conv}}(\ell) \geq i_{\mathrm{conv},x}(\ell) - i_{\mathrm{conv,max}} \tag{13a}$$
$$\xi_{\mathrm{conv}}(\ell) \geq -i_{\mathrm{conv},x}(\ell) - i_{\mathrm{conv,max}} \tag{13b}$$
$$\xi_{\mathrm{conv}}(\ell) \geq 0\,, \tag{13c}$$

where the slack variable ξ_{conv} maps the constraint violation into a nonnegative real number. Note that due to three-phase symmetry, $i_{\mathrm{conv,max}}$ defines both upper and lower bounds, i.e., the trip levels to limit the 3L-NPC switch stress.

For each single-phase component, the three constraints define three lines which restrict the feasible space of the slack variable, indicated by the shaded area in Fig. 3. The slope of the soft constraints relates to the penalty used to weigh $\xi_{\mathrm{conv}}(\ell)$, thus, by heavily penalizing such constraints—effectively—very steep slopes result. In doing so, the implemented soft constraints can keep $i_{\mathrm{conv},x}(\ell)$ within the desired limits almost as strictly as hard constraints, while guaranteeing that potential numerical and/or feasibility issues do not arise. Such constraints in vector form can be written as

$$\mathbf{1}_7\xi_{\mathrm{conv}}(\ell) \succeq \boldsymbol{W}\boldsymbol{K}^{-1}\boldsymbol{i}_{\mathrm{conv}}(\ell) - \begin{bmatrix}\mathbf{1}_6\\ 0\end{bmatrix} i_{\mathrm{conv,max}}\,, \tag{14}$$

with $\boldsymbol{K}^{-1}$ being the pseudoinverse of the (reduced) Clarke transformation, and

$$\boldsymbol{W} = \begin{bmatrix}1 & -1 & 0 & 0 & 0 & 0 & 0\\ 0 & 0 & 1 & -1 & 0 & 0 & 0\\ 0 & 0 & 0 & 0 & 1 & -1 & 0\end{bmatrix}^T.$$

Similar to (14), upper and lower constraints are imposed on the capacitor voltage, with $v_{c,\max}$ referring to ξ_c, and on the grid current, with $i_{g,\max}$ to ξ_g. By aggregating the slack variables in the vector

$$\boldsymbol{\xi}(\ell) = [\xi_{\mathrm{conv}}(\ell)\ \xi_c(\ell)\ \xi_g(\ell)]^T\,, \tag{15}$$

the soft constraints on all variables of interest are written as

$$\boldsymbol{M}\boldsymbol{\xi}(\ell) \succeq \widetilde{\boldsymbol{W}}\widetilde{\boldsymbol{K}}\boldsymbol{C}\boldsymbol{x}(\ell) - \boldsymbol{N}\boldsymbol{c}\,, \tag{16}$$

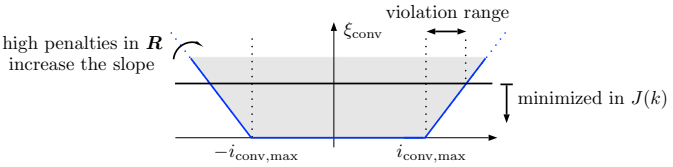

Fig. 3. Soft constraints applied on $i_{\mathrm{conv},a}(\ell)$ at each time step ℓ through the slack variable $\xi_{\mathrm{conv}}(\ell)$, for which the feasible space is restricted by the blue lines. The black line denotes the optimal value $\xi^*_{\mathrm{conv}}(\ell)$ which is computed by solving the complete optimization problem (18).

where $\boldsymbol{c} = [i_{\mathrm{conv,max}}\ v_{c,\max}\ i_{g,\max}]^T$ and

$$\boldsymbol{M} = \begin{bmatrix}\mathbf{1}_7 & \mathbf{0}_7 & \mathbf{0}_7\\ \mathbf{0}_7 & \mathbf{1}_7 & \mathbf{0}_7\\ \mathbf{0}_7 & \mathbf{0}_7 & \mathbf{1}_7\end{bmatrix},\quad \boldsymbol{N} = \begin{bmatrix}\mathbf{1}_6 & 0 & \mathbf{0}_6 & 0 & \mathbf{0}_6 & 0\\ \mathbf{0}_6 & 0 & \mathbf{1}_6 & 0 & \mathbf{0}_6 & 0\\ \mathbf{0}_6 & 0 & \mathbf{0}_6 & 0 & \mathbf{1}_6 & 0\end{bmatrix}^T,$$

$$\widetilde{\boldsymbol{W}} = \mathrm{diag}\,(\boldsymbol{W}, \boldsymbol{W}, \boldsymbol{W})\,,\quad \widetilde{\boldsymbol{K}} = \mathrm{diag}\left(\boldsymbol{K}^{-1}, \boldsymbol{K}^{-1}, \boldsymbol{K}^{-1}\right).$$

C. Optimization Problem

To minimize the slack variables, avoiding as much violation of the (soft) output constraints as possible, the term

$$\sum_{\ell=k}^{k+N_p-1} \|\boldsymbol{\xi}(\ell+1)\|^2_{\boldsymbol{R}} \tag{17}$$

is added to (9) and weighted with the penalty matrix $\boldsymbol{R} \succeq 0$. Thus the objective function becomes

$$J(k) = \sum_{\ell=k}^{k+N_p-1} \|\boldsymbol{y}_{\mathrm{err}}(\ell+1)\|^2_{\boldsymbol{Q}} + \lambda_u \|\Delta\boldsymbol{u}(\ell)\|_2^2 + \|\boldsymbol{\xi}(\ell)\|^2_{\boldsymbol{R}}\,. \tag{18}$$

In (18) the weighting matrices $\boldsymbol{Q}$, $\boldsymbol{R}$, and the weighting factor λ_u prioritize among the conflicting goals of the controller. Large positive values are chosen for $\boldsymbol{R}$, penalizing heavily the slack variables in $J(k)$ so as to get as close to the behavior achieved with hard constraints as possible.

By introducing the sequence of slack variables over the prediction horizon as

$$\boldsymbol{\Xi}(k) = [\boldsymbol{\xi}^T(k+1)\ \boldsymbol{\xi}^T(k+2)\ \ldots\ \boldsymbol{\xi}^T(k+N_p)]^T \tag{19}$$

the optimization variable becomes

$$\widetilde{\boldsymbol{U}}(k) = \left[\boldsymbol{U}^T(k)\ \boldsymbol{\Xi}^T(k)\right]^T. \tag{20}$$

As there are three manipulated variables and three slack variables at each time step, the optimization vector is of the dimension $6N_p$, thus, $\widetilde{\boldsymbol{U}}(k) \in \mathbb{R}^{6N_p}$. Based on the above, the optimization problem takes the form

$$\underset{\widetilde{\boldsymbol{U}}(k)\in\mathbb{R}^{6N_p}}{\text{minimize}}\ \ J(k) \tag{21a}$$
$$\text{subject to}\ \ \boldsymbol{x}(\ell+1) = \boldsymbol{A}\boldsymbol{x}(\ell) + \boldsymbol{B}\boldsymbol{u}(\ell) \tag{21b}$$
$$\boldsymbol{y}(\ell+1) = \boldsymbol{C}\boldsymbol{x}(\ell+1) \tag{21c}$$
$$\Delta\boldsymbol{u}(\ell) = \boldsymbol{u}(\ell) - \boldsymbol{u}(\ell-1) \tag{21d}$$
$$\widetilde{\boldsymbol{W}}\widetilde{\boldsymbol{K}}\boldsymbol{C}\boldsymbol{x}(\ell+1) - \boldsymbol{M}\boldsymbol{\xi}(\ell+1) \preceq \boldsymbol{N}\boldsymbol{c} \tag{21e}$$
$$\boldsymbol{V}\boldsymbol{u}(\ell) \preceq \mathbf{1}_6 \tag{21f}$$
$$\forall \ell = k, \ldots, k+N_p-1\,.$$

As function (18) is quadratic and subjected to the evolution of a linear state-space model with linear inequality constraints, the resulting optimization problem is a QP. In particular, (21)

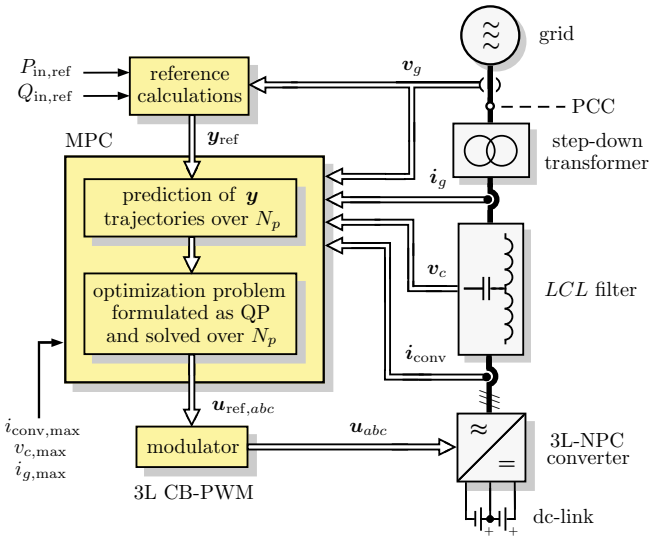

Fig. 4. Indirect MPC formulated as a multi-criterion QP for the ac-dc conversion system shown in Fig. 1(a). The output references are computed from the power demand; a 3L CB-PWM is included.

is a strictly convex QP since the Hessian matrix is positive definite [15], as shown in the following. Note that since V_{dc} is time invariant the optimization problem is time invariant as well. The QP can be solved efficiently on embedded hardware by using off-the-shelf solvers, e.g., [9]–[11], which speed-up computations.

The result of the optimization stage is the sequence of optimal manipulated variables $\widetilde{\boldsymbol{U}}^*(k)$ at time step k, i.e.,

$$\widetilde{\boldsymbol{U}}^*(k) = \Big[\widetilde{\boldsymbol{u}}^{*T}(k)\ \widetilde{\boldsymbol{u}}^{*T}(k+1)\ \ldots\ \widetilde{\boldsymbol{u}}^{*T}(k+N_p-1)\Big]^T. \quad (22)$$

Out of this sequence the first element $\boldsymbol{u}^*(k)$, i.e., the optimal modulating signal at time step k, is fed into the 3L CB-PWM stage, while the rest are discarded in line with the receding horizon control principle [16]. The proposed approach is summarized by the scheme in Fig. 4.

D. Optimization Problem in Vector Form

To write the QP in a form suitable for embedded implementation the optimization problem has to be rewritten in a vector form. Considering the output reference over the horizon

$$\boldsymbol{Y}_{\text{ref}}(k) = [\boldsymbol{y}_{\text{ref}}^T(k+1)\ \boldsymbol{y}_{\text{ref}}^T(k+2)\ \ldots\ \boldsymbol{y}_{\text{ref}}^T(k+N_p)]^T, \quad (23)$$

and after some algebraic manipulations, function (18) can be written in a vector form as

$$\begin{aligned} J(k) = &\|\boldsymbol{Y}_{\text{ref}}(k) - \boldsymbol{\Gamma}\boldsymbol{x}(k) - \boldsymbol{\Upsilon}\boldsymbol{U}(k)\|^2_{\widetilde{\boldsymbol{Q}}} \\ &+ \lambda_u \|\boldsymbol{S}\boldsymbol{U}(k) - \boldsymbol{E}\boldsymbol{u}(k-1)\|_2^2 + \|\boldsymbol{\Xi}(k)\|^2_{\widetilde{\boldsymbol{R}}}\,, \end{aligned} \quad (24)$$

where $\widetilde{\boldsymbol{Q}} = \text{diag}\,(\boldsymbol{Q},\ldots,\boldsymbol{Q})$ and $\widetilde{\boldsymbol{R}} = \text{diag}\,(\boldsymbol{R},\ldots,\boldsymbol{R})$, while matrices $\boldsymbol{\Gamma}$, $\boldsymbol{\Upsilon}$, $\boldsymbol{S}$ and $\boldsymbol{E}$ can be found in [5, Appendix 5.B]. By introducing the matrices and variable

$$\begin{aligned} \boldsymbol{Z} &= \boldsymbol{\Upsilon}^T\widetilde{\boldsymbol{Q}}\boldsymbol{\Upsilon} + \lambda_u \boldsymbol{S}^T\boldsymbol{S} \\ \boldsymbol{\theta}(k) &= -\boldsymbol{\Upsilon}^T\widetilde{\boldsymbol{Q}}\,(\boldsymbol{Y}_{\text{ref}}(k) - \boldsymbol{\Gamma}\boldsymbol{x}(k)) - \lambda_u \boldsymbol{S}^T\boldsymbol{E}\boldsymbol{u}(k-1) \\ \theta(k) &= \|\boldsymbol{Y}_{\text{ref}}(k) - \boldsymbol{\Gamma}\boldsymbol{x}(k)\|^2_{\widetilde{\boldsymbol{Q}}} + \lambda_u \|\boldsymbol{E}\boldsymbol{u}(k-1)\|_2^2\,, \end{aligned}$$

function (24) is rewritten as[9]

$$\begin{aligned} J(k) &= \boldsymbol{U}^T(k)\boldsymbol{Z}\boldsymbol{U}(k) + \boldsymbol{\Xi}^T(k)\widetilde{\boldsymbol{R}}\boldsymbol{\Xi}(k) + 2\boldsymbol{\theta}^T(k)\boldsymbol{U}(k) \\ &= \widetilde{\boldsymbol{U}}(k)\boldsymbol{H}\widetilde{\boldsymbol{U}}(k) + 2\boldsymbol{d}^T(k)\widetilde{\boldsymbol{U}}(k)\,, \end{aligned} \quad (26)$$

where the Hessian matrix $\boldsymbol{H} \succ 0$ is the block diagonal matrix $\boldsymbol{H} = \text{diag}(\boldsymbol{Z}, \widetilde{\boldsymbol{R}})$ and $\boldsymbol{d}(k) = [\boldsymbol{\theta}^T(k)\ \boldsymbol{0}^T_{3N_p}]^T$.

The input constraints in (21) in vector form are

$$\begin{aligned} \boldsymbol{\Omega}\boldsymbol{U}(k) &\preceq \boldsymbol{1}_{6N_p} \Leftrightarrow \\ \big[\boldsymbol{\Omega}\ \boldsymbol{0}_{6N_p\times 3N_p}\big]\,\widetilde{\boldsymbol{U}}(k) &\preceq \boldsymbol{1}_{6N_p}\,, \end{aligned} \quad (27)$$

where $\boldsymbol{\Omega} = \text{diag}\,(\boldsymbol{V},\ldots,\boldsymbol{V})$, while the output constraints can be written as

$$\begin{aligned} \boldsymbol{Z}\boldsymbol{\Xi}(k) &\preceq \boldsymbol{\Delta} - \boldsymbol{\Pi}\,(\boldsymbol{\Gamma}\boldsymbol{x}(k) + \boldsymbol{\Upsilon}\boldsymbol{U}(k)) \Leftrightarrow \\ \boldsymbol{Z}\boldsymbol{\Xi}(k) + \boldsymbol{\Pi}\boldsymbol{\Upsilon}\boldsymbol{U}(k) &\preceq \boldsymbol{\Delta} - \boldsymbol{\Pi}\boldsymbol{\Gamma}\boldsymbol{x}(k) \Leftrightarrow \\ [\boldsymbol{\Pi}\boldsymbol{\Upsilon}\ \boldsymbol{Z}]\,\widetilde{\boldsymbol{U}}(k) &\preceq \boldsymbol{\Delta} - \boldsymbol{\Pi}\boldsymbol{\Gamma}\boldsymbol{x}(k)\,, \end{aligned} \quad (28)$$

where the matrices $\boldsymbol{Z}$, $\boldsymbol{\Pi}$, and $\boldsymbol{\Delta}$ are defined as

$$\begin{aligned} \boldsymbol{Z} &= \text{diag}\,(-\boldsymbol{M},\ldots,-\boldsymbol{M})\,, \\ \boldsymbol{\Pi} &= \text{diag}\left(\widetilde{\boldsymbol{W}}\widetilde{\boldsymbol{K}},\ldots,\widetilde{\boldsymbol{W}}\widetilde{\boldsymbol{K}}\right), \\ \boldsymbol{\Delta} &= \big[\,\boldsymbol{N}\boldsymbol{c}\ \ldots\ \boldsymbol{N}\boldsymbol{c}\,\big]^T. \end{aligned}$$

By combining (27) and (28) into one expression, the optimization problem (21) takes its final form suitable for embedded implementation, i.e.,

$$\begin{aligned} &\underset{\widetilde{\boldsymbol{U}}(k)\in\mathbb{R}^{6N_p}}{\text{minimize}}\ \ \widetilde{\boldsymbol{U}}(k)\boldsymbol{H}\widetilde{\boldsymbol{U}}(k) + 2\boldsymbol{d}^T(k)\widetilde{\boldsymbol{U}}(k) \\ &\text{subject to}\ \begin{bmatrix}\boldsymbol{\Omega} & \boldsymbol{0}_{6N_p\times 3N_p}\\ \boldsymbol{\Pi}\boldsymbol{\Upsilon} & \boldsymbol{Z}\end{bmatrix}\widetilde{\boldsymbol{U}}(k) \preceq \begin{bmatrix}\boldsymbol{1}_{6N_p}\\ \boldsymbol{\Delta}-\boldsymbol{\Pi}\boldsymbol{\Gamma}\boldsymbol{x}(k)\end{bmatrix}. \end{aligned} \quad (30)$$

As a result, the QP in the form (30) facilitates the real-time implementation of the proposed MPC algorithm.

In this direction, some preliminary tests have been done with a Xilinx system-on-chip field-programmable gate array (SoC FPGA). For instance, (30) has been implemented on the ARM R5 processor of a Zynq UltraScale+ MPSoC ZU9EG, and qpOASES, i.e., an online active-set method based solver [11], was employed to solve the underlying QP.

V. Performance Evaluation

The performance of the proposed indirect MPC scheme is evaluated at steady-state operating conditions and during transients through MATLAB simulations. The system parameters are given in Table I. The MPC scheme is executed at the (upper and lower) peaks of the triangular carrier, with $f_c = 750\,\text{Hz}$, implying a sampling interval of $T_s = 1/(2f_c) = 666.67\,\mu\text{s}$. According to Table I, the dominant resonance frequency is $f_{\text{res}} = 304\,\text{Hz}$. The prediction horizon is $N_p = 4$. Shorter horizons might adversely affect the closed-loop system stability, hence, a relatively long prediction horizon—combined with the full-state information of MPC—can render an additional active damping loop unnecessary [6], [17]. Note that the full

[9]Note that in (26) the coefficient $\theta(k)$ is omitted since it merely adds an offset to the total cost, i.e., $J(k) = \boldsymbol{U}^T(k)\boldsymbol{Z}\boldsymbol{U}(k) + \boldsymbol{\Xi}^T(k)\widetilde{\boldsymbol{R}}\boldsymbol{\Xi}(k) + 2\boldsymbol{\theta}^T(k)\boldsymbol{U}(k) + \theta(k)$.

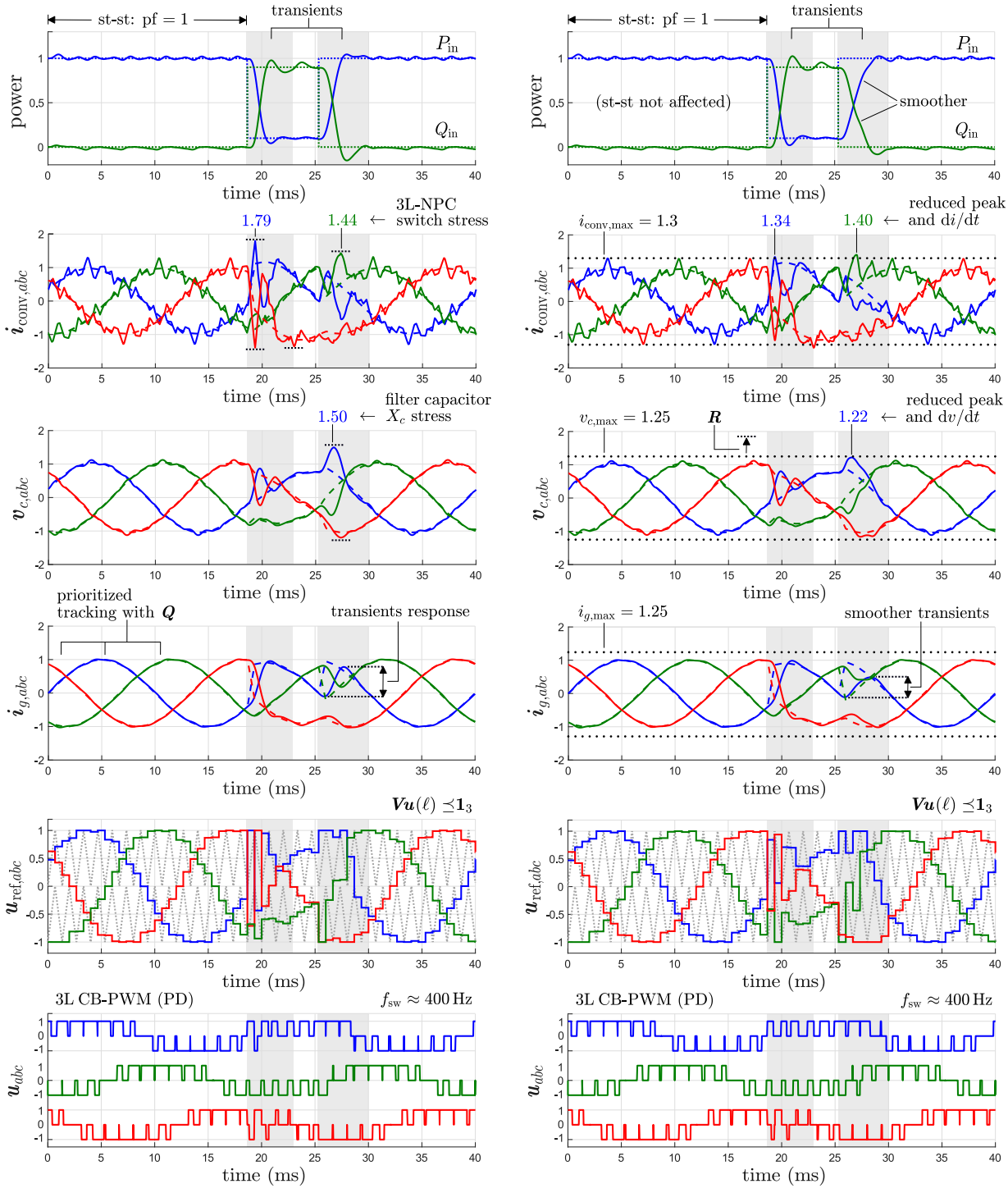

(a) (b)

Fig. 5. Simulated waveforms produced by indirect MPC with $N_p = 4$, when the soft constraints are (a) not included (b) included. The results are shown over two fundamental periods $2T_g$, with $T_g = 1/f_g = 20\,\text{ms}$. Both steady-state and transient operations are tested. From top to bottom: real power $P_{\text{in}}(t)$ (blue line) and reactive power $Q_{\text{in}}(t)$ (green line) and their references (dashed lines); three-phase converter input currents $\boldsymbol{i}_{\text{conv},abc}(t)$ (with phase a, b and c denoted as blue, red and green lines, respectively) and the related references; three-phase capacitor voltage $\boldsymbol{v}_{c,abc}(t)$; three-phase grid currents $\boldsymbol{i}_{g,abc}(t)$; three-phase modulating signal $\boldsymbol{u}_{abc,\text{ref}}(t)$ along with the two carrier waveforms (gray dotted lines); three-phase switch positions $\boldsymbol{u}_{abc}$.

state $\boldsymbol{x}$ is measured[10] and assumed to be available to the controller along with $\boldsymbol{y}_{\text{ref}}$. Moreover, the implemented control action is fed into the modulator and kept constant between time steps k and $k+1$. Regarding the modulator, asymmetric regularly sampled 3L CB-PWM with PD is used. Finally, all results are presented in the p.u. system.

[10]Computational delays are assumed to be fully compensated for.

A. Choice of the Design Parameters

The main goal of the tuning procedure is to prioritize the grid current reference tracking to reduce the grid current TDD, $I_{g,\text{TDD}}$, while minimizing the violation of the soft constraints. Hence, the error $\boldsymbol{i}_{g,\text{ref}}(\ell+1) - \boldsymbol{i}_g(\ell+1)$ is prioritized over the error of the other controlled variables by imposing a much bigger penalty on the associated entries of

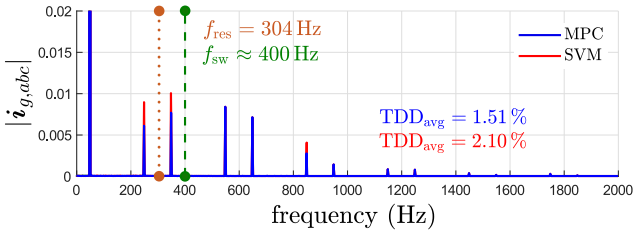

(a)

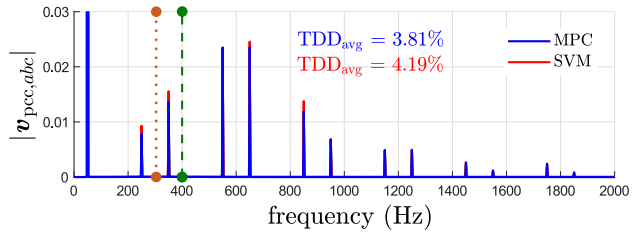

(b)

Fig. 6. Harmonic spectra of the (a) grid current, and (b) PCC voltage. For both cases, the harmonics do not violate their respective limits imposed by the IEEE 519 and IEC 61000-2-4 standards, respectively.

TABLE I
MV SYSTEM PARAMETERS

Rated values		Parameters	
Input voltage V_R	3.3 kV	Filter inductance L_{fg}	0.403 mH
Input current I_R	1575 A	Filter resistance R_{fg}	0.484 mΩ
Apparent power S_R	9 MVA	Filter inductance L_{fc}	0.452 mH
Grid frequency f_g	50 Hz	Filter resistance R_{fc}	0.484 mΩ
Dc-link voltage V_{dc}	5.4 kV	Filter capacitance C	884.9 μF
Dc capacitor C_{dc}	15 mF	Filter resistance R_c	0.484 mΩ
Grid inductance L_g	0.192 mH	Leakage inductance L_t	0.385 mH
Grid resistance R_g	6.019 mΩ	Leakage resistance R_t	10.10 mΩ

$\boldsymbol{Q}$. Given this, the weighting matrix of the output error term is chosen as $\boldsymbol{Q} = \text{diag}\,(10, 10, 1, 1, 100, 100)$. Furthermore, the weighting factor on the manipulated variable is chosen as $\lambda_u = 1$ to prevent aggressive control actions during transients. As for the soft constraints, these are activated at $i_{\text{conv,max}} = 1.3\,\text{p.u.}$, $v_{c,\text{max}} = 1.25\,\text{p.u.}$, and $i_{g,\text{max}} = 1.25\,\text{p.u.}$ To ensure that the latter are not violated during transients, high values are assigned to the nonzero entries of $\boldsymbol{R}$, i.e., $\boldsymbol{R} = \text{diag}\,(10^5, 10^5, 1)$. Note that since the grid current tracking is prioritized with $\boldsymbol{Q}$, big deviations—and thus overcurrents—of the grid current are already penalized, thus, a high penalty on ξ_g is redundant.

B. Steady-State Operation

The steady-state performance of the proposed indirect MPC is shown in Fig. 5. More specifically, Fig. 5(a) shows the system behavior when the soft constraints are not included in the MPC problem, whereas Fig. 5(b) depicts the system response when the aforementioned constraints are taken into account. In both cases, operation at nominal active power and zero reactive power is considered, i.e., $P_{\text{in,ref}}(t) = 1$ and $Q_{\text{in,ref}}(t) = 0$ with $\text{pf} = 1$. As can be seen in Fig. 5, all output variables $\boldsymbol{y}$ accurately track their reference values. Hence, they are effectively sinusoidal, despite operation at a low switching frequency of $f_{\text{sw}} = 400\,\text{Hz}$. Note that the latter is close to the resonance frequency f_{res}. It is worth mentioning that the soft constraints (shown as black dotted lines in Fig. 5(b)) are not activated during steady-state operation, hence the MPC algorithm performs the same, whether there are soft constraints or not. On the other hand, the constraints on the control input, i.e., the three-phase modulating signal $\boldsymbol{u}_{abc,\text{ref}}(t)$, are activated and fully respected since they are implemented as hard constraints. In doing so, the instantaneous values of the modulating signal are always less than the peak values of the triangular carries and the comparisons in line with the CB-PWM principle can be successfully performed. Hence, by driving this signal to the subsequent modulation stage, the three-phase switch positions–which are applied to the converter—are generated, see the last row of figures in Fig. 5.

To assess whether the grid current and PCC voltage produced by the proposed MPC algorithm meet the grid standards, the relevant harmonic spectra are examined. To this aim, Fig. 6(a) shows the harmonic spectrum of the grid current $\boldsymbol{i}_{g,abc}(t)$. As mentioned above, it can be observed that despite the very low switching frequency—which is very close to the resonance frequency—the grid current distortions are very low, resulting in a TDD value of $I_{g,\text{TDD}} = 1.51\%$. Moreover, the harmonics are at odd, non-triplen multiplies of the fundamental frequency, with sidebands around the carrier frequency. Given that $k_{\text{sc}} \approx 19.96$, the IEEE 519 standard indicates a maximum $I_{g,\text{TDD,max}} = 8\%$ with the tighter limits imposed above the 35^{th} harmonic. Thus, the stringent limits on the grid current harmonics are adhered to. Likewise, Fig. 6(b) shows the spectrum of the voltage at the PCC along with its (low) TDD value. Given the limitations imposed by the IEC 61000-2-4 for a Class 2 electromagnetic environment, it can be concluded that they are fully respected.

Based on the above results, it can be claimed that the proposed controller can produce grid currents with low distortions (i.e., low $I_{g,\text{TDD}}$) and without exciting the resonance frequency. This outcome is achieved without the existence of an additional outer damping loop and while no passive damping is provided by the system components. Specifically, the controller shapes the grid current spectrum by utilizing the information extracted from the internal prediction model used to evaluate the system behavior over a (sufficiently long) horizon of N_p time steps. Therefore, the converter can be successfully operated at switching frequencies close to the resonance frequency, while meeting the standards. In doing so, the switching losses are also kept low.

Finally, as a benchmark, convectional CB-PWM with min/max common-mode signal injection is used, which is equivalent to space vector modulation (SVM) [13]. Moreover, for a fair comparison, operation at the same f_{sw} is considered. This can be interpreted as having a simple closed-loop linear controller with a very low bandwidth. As can be seen in Fig. 6(a), the grid current harmonics produced by SVM are of the same order, but slightly different amplitude, compared with those of indirect MPC. As a result, the grid current TDD with SVM is slightly higher ($I_{g,\text{TDD}} = 2.01\%$) than that of MPC. The same trend is observed in the harmonic spectrum of the voltage at the PCC, see Fig. 6(b); as with the grid current, the voltage harmonics are similar but of slightly higher amplitude, giving rise to a voltage TDD of 4.19%.

C. Transient Operation

To investigate the dynamic behavior of the closed-loop system, input power reference steps are applied. At 18 ms, $P_{\mathrm{in,ref}}(t)$ is changed from 1 to 0.2 p.u. and back to 1 p.u. at $t = 26$ ms. Likewise, $Q_{\mathrm{in,ref}}(t)$ is changed from 0 to 0.8 p.u. and back to 0 p.u. at the same time instants. These transients are indicating a high stress in the grid due to a large load demand. As can be seen in both Figs. 5(a) and 5(b), the controlled variables—and consequently the powers—accurately follow their references.

The ability of the proposed MPC algorithm to respect operational constraints on the output variables can be appreciated by comparing Fig. 5(a) (i.e., MPC without soft constraints) with Fig. 5(b) (i.e., MPC with soft constraints). As can be seen, in the former figure, the variables $\boldsymbol{i}_{\mathrm{conv}}(t)$ and $\boldsymbol{v}_c$(t) exhibit significant overshoots during transients, violating the associated trip levels. For instance, peak values $i_{\mathrm{conv},a}(t) = 1.79$ p.u. and $i_{\mathrm{conv},c}(t) = 1.44$ p.u. are 49% and 14% above $i_{\mathrm{conv,max}} = 1.3$ p.u., respectively, while the trip levels violations occur over an interval of 330 μs for phase a and 540 μs for phase c. Note that such current excursions may damage the hardware, thus they should be avoided. Similar considerations apply to the capacitor voltage, which presents a peak of $v_{c,a}(t) = 1.50$ p.u., and an overvoltage time interval of 990 μs given that $v_{\mathrm{c,max}} = 1.25$ p.u. Such conditions may have a strong impact on the capacitor electro-thermal stresses.

On the other hand, when the MPC problem (30) is implemented, the soft constraints on the output variables are activated, see Fig. 5(b). As can be observed, due to the heavy penalization of the associated slack variables, all controlled variables remain mostly within their bounds, with minute violations occurring in the converter current. Notwithstanding the foregoing, overcurrents and/or overvoltages are prevented, thus the hardware of the system is protected from potential damages and/or trips. It is worth mentioning, however, that when the soft constraints are included in the optimization problem the controller is less aggressive since it tries to keep the controlled variables within their safety limits. As a result, the settling time of the power transient during the step-down change in $P_{\mathrm{in,ref}}$ is about 2 ms when the constraints are not taken into account, as opposed to 2.2 ms, which is the time required from the constrained MPC. As for the step-up change in $P_{\mathrm{in,ref}}$, the unconstrained MPC requires 3 ms to settle to the new operating point, i.e., longer than before due to the limited available voltage margin, whereas the transient time with the constrained MPC is 3.98 ms. Both methods, however, try to eliminate the output tracking error as quickly as possible. This is evident from the computed control input (i.e., modulating signal) which is saturated at the corresponding maximal/minimal allowable values, see the second to bottom row of figures in Figs. 5(a) and 5(b).

VI. Conclusions

This paper presented a long-horizon MPC algorithm with a modulator for a 3L-NPC converter connected to the grid via an intermediate LCL filter. By appropriately formulating the optimization problem underlying indirect MPC as a multi-criterion QP, the grid and converter currents as well as the filter capacitor voltage can be successfully controlled, while the relevant grid standards, e.g., IEEE 519 and IEC 6000-2-4, can be met. The above can be achieved while respecting the trip/protection levels of the system, thus enhancing the converter reliability. To realize the latter, soft constraints are included into the optimization problem, the violation of which is minimized. To this end, MPC computes the optimal three-phase modulating signal—subsequently fed into a CB-PWM stage—that satisfies all the aforementioned objectives and ensures smooth operation of the system. Finally, a relatively long prediction horizon is employed to improve the closed-loop system performance and avoid potential stability issues. The effectiveness of the proposed strategy was evaluated through simulations both at steady-state and transient operation. As shown, the converter can be operated at a switching frequency of a few hundred Hz, very close to the resonance frequency, without requiring an additional active damping loop.

References

[1] IEEE Std 519-2014 (Revision of IEEE Std 519-1992), "IEEE recommended practices and requirements for harmonic control in electrical power systems," pp. 1–29, Jun. 2014.

[2] IEC 61000-2-4, "Electromagnetic compatibility (EMC)—part 2-4: Environment—compatibility levels in industrial plants for low-frequency conducted disturbances," Sep. 2002.

[3] P. Cortés, M. P. Kazmierkowski, R. M. Kennel, D. E. Quevedo, and J. Rodríguez, "Predictive control in power electronics and drives," *IEEE Trans. Ind. Electron.*, vol. 55, no. 12, pp. 4312–4324, Dec. 2008.

[4] J. Rodríguez, M. P. Kazmierkowski, J. R. Espinoza, P. Zanchetta, H. Abu-Rub, H. A. Young, and C. A. Rojas, "State of the art of finite control set model predictive control in power electronics," *IEEE Trans. Ind. Informat.*, vol. 9, no. 2, pp. 1003–1016, May 2013.

[5] T. Geyer, *Model predictive control of high power converters and industrial drives*. Hoboken, NJ: Wiley, 2016.

[6] P. Karamanakos and T. Geyer, "Guidelines for the design of finite control set model predictive controllers," *IEEE Trans. Power Electron.*, vol. 35, no. 7, pp. 7434–7450, Jul. 2020.

[7] P. Karamanakos, T. Geyer, N. Oikonomou, F. D. Kieferndorf, and S. Manias, "Direct model predictive control: A review of strategies that achieve long prediction intervals for power electronics," *IEEE Ind. Electron. Mag.*, vol. 8, no. 1, pp. 32–43, Mar. 2014.

[8] T. Geyer, P. Karamanakos, and R. Kennel, "On the benefit of long-horizon direct model predictive control for drives with LC filters," in *Proc. IEEE Energy Convers. Congr. Expo.*, Pittsburgh, PA, Sep. 2014, pp. 3520–3527.

[9] B. Hauska, H. J. Ferreau, and M. Diehl, "An auto-generated real-time iteration algorithm for nonlinear MPC in the microsecond range," *Automatica*, vol. 47, no. 10, pp. 2279–2285, Oct. 2011.

[10] H. Peyrl, A. Zanarini, T. Besselmann, J. Liu, and M.-A. Boéchat, "Parallel implementations of the fast gradient method for high-speed MPC," *Control Eng. Pract.*, vol. 33, pp. 22–34, Dec. 2014.

[11] H. J. Ferreau, C. Kirches, A. Potschka, H. G. Bock, and M. Diehl, "qpOASES: A parametric active-set algorithm for quadratic programming," *Math. Program. Comp.*, vol. 6, no. 4, pp. 327–363, Dec. 2014.

[12] S. Yang, A. Bryant, P. Mawby, D. Xiang, L. Ran, and P. Tavner, "An industry-based survey of reliability in power electronic converters," *IEEE Trans. Ind. Appl.*, vol. 47, no. 3, pp. 1441–1451, 2011.

[13] D. G. Holmes and T. A. Lipo, *Pulse width modulation for power converters: Principles and practice*. Piscataway, NJ: IEEE Press, 2003.

[14] G. Darivianakis, T. Geyer, and W. van der Merwe, "Model predictive current control of modular multilevel converters," in *Proc. IEEE Energy Convers. Congr. Expo.*, Pittsburgh, PA, Sep. 2014, pp. 5016–5023.

[15] S. Boyd and L. Vandenberghe, *Convex optimization*. Cambridge, UK: Cambridge Univ. Press, 2004.

[16] J. B. Rawlings and D. Q. Mayne, *Model predictive control: Theory and design*. Madison, WI: Nob Hill, 2009.

[17] P. Karamanakos, M. Nahalparvari, and T. Geyer, "Fixed switching frequency direct model predictive control with continuous and discontinuous modulation for grid-tied converters with LCL filters," *IEEE Trans. Control Syst. Technol.*, pp. 1–16, 2020, in press, DOI: 10.1109/TCST.2020.3008030.